Understanding the Effect of Antisolvent on Processing Window and Efficiency for Large-area Flexible Perovskite Solar Cells

Cong Chen [a, b], Yue Jiang [a*], Yancong Feng [a*], Zhuoxi Li [a], Nengjie Cao [c], Guofu Zhou [c], Jun-Ming Liu [d], Krzysztof Kempa [e], Shien-Ping Feng [b*], Jinwei Gao [a*]

[a] Institute for Advanced Materials, South China Academy of Advanced Optoelectronics, and Guangdong Provincial Key Laboratory of Optical Information Materials and Technology, South China Normal University, Guangzhou 510006, China.

[b] Department of Mechanical Engineering, The University of Hong Kong, Pokfulam Rd., Pokfulam, Hong Kong.

[c] Guangdong Provincial Key Laboratory of Optical Information Materials and Technology & Institute of Electronic Paper Displays, South China Academy of Advanced Optoelectronics, South China Normal University, Guangzhou 510006, China.

[d] Laboratory of Solid-State Microstructures, Nanjing University, Nanjing 210093, China.

[e] Department of Physics, Boston College, Chestnut Hill, Massachusetts 02467, USA

*Corresponding Author

E-mail: yuejiang@m.scnu.edu.cn (Y.J.), fengyancong@m.scnu.edu.cn (Y.F.), hpfeng@hku.hk (S.F), gaojinwei@m.scnu.edu.cn (J.G.),

Keywords: Antisolvent, Processing window, Large-area, Perovskite solar cells

Abstract:

One-step method assisted by antisolvent is the most useful strategy to fabricate perovskite solar cells (PSCs) with high power conversion efficiency (PCE). Nevertheless, the narrow processing window and strict solvent ratio restricts the fabrication of large-area and uniform perovskite films. Herein, by thoroughly investigating the interaction between solvents and antisolvents during the processing, we discover the significant role of the typical solvent of dimethylformamide in the process of antisolvent washing and we demonstrate a solvent-antisolvent interaction model to understand the originality of narrow processing window and solvent ratio based on chlorobenzene. Furthermore, we introduce a green antisolvent —— Ethyl Methyl Carbonate, with a large processing window from 2s to 35s, and a prolonged dimethylformamide: dimethyl sulfoxide volume ration varying from 7:3 to 0:10 in the precursor solution. The obtained PSCs show remarkable efficiency of 22.08% on rigid substrates, and 19.14% on flexible substrates. In a parallel effort, we demonstrate a uniform and large-area (6×6 cm^2) flexible perovskite film, exhibiting the highest PCE

of 18.60%.

1. Introduction

organic–inorganic hybrid perovskite solar cell (PSC) have been intensively investigated as a promising candidate for the next-generation photovoltaic devices, which provided affordable and clean energy with the certified power-conversion efficiency (PCE) over 25% [1–3]. This significant progress relies on superior inherent properties of perovskite materials such as the high absorption coefficient, long carrier lifetimes (up to 30 μs), large carrier diffusion length (>1 μm) and low exciton binding energy as well as various methods of depositing perovskite film including vacuum vapor deposition and one-step/two-step solution deposition technologies [4–9].

Among the above methods, one-step antisolvent assisted solution technology is an effective and widely adopted approach to obtain a dense and highly crystallized solution-processed perovskite film, which is paramount in determining the device performances[10–14]. Antisolvent could extract solute from the precursor, thus forming a driving force towards the formation of intermediate phase from this supersaturated solution [15–19]. The commonly used antisolvents include chlorobenzene (CB) [20], toluene (TL) [16] and diethyl ether (DE) [21]. However, apart from their toxicity, these antisolvents are facing severe problems, including the extremely narrow processing window which is severely relied on two parameters: (1) the ratio of DMF/DMSO needs to be precisely optimized within a narrow range for different antisolvents. For instance, the proper volume ration for CB is 4:1[22], TL is

7:3 [8] and DE is 9:1 [21]; (2) the antisolvent has to be dripped at specific time slot (8-10th s) after the spin coating procedure starts. Otherwise, the obtained perovskite film show low quality with high roughness, high-density pin-hole, and low coverage, seriously limiting the reproducibility of efficient PSCs [19,23–25].

Various strategies have been employed to prolong the processing window of one-step antisolvent method for efficient and large-area PSCs fabrications. Precursor addictive methods including methylammonium chloride, diphenyl sulfoxide and crown have been reported for enabling a wide antisolvent processing time [26–28]. Meanwhile, alternative antisolvents, such as tert-butyl alcohol and anisole, have been used to effectively prolong the processing window, owning to the presence of intermolecular forces between antisolvent and precursor solvent [15,23,24,29]. Nevertheless, few research has revealed the critical mechanism of that super narrow processing window based on CB antisolvent, consequently leading to deficiently understand the role of solvents and antisolvent in the film forming process [30].

In this article, we firstly, systematically investigate the formation of perovskite film under different solvents and antisolvents, and then disclose the significant role of the typical solvent of DMF in the process of antisolvent washing, with a reasonable solvent–antisolvent interaction model. Finally, we have discovered a green antisolvent of ethyl methyl carbonate (EMC), with a significantly prolonged antisolvent processing window from 2 s to 35 s, as well as a wide dimethylformamide (DMF):dimethyl sulfoxide (DMSO) volume ratio varying from 7:3 to 0:10 in the precursor solution. We demonstrate perovskite solar cells based on EMC antisolvent that show a maximum PCE of 21.05% and 22.08% for $MAPbI_3$ and $(MA)_x(FA)_{(1-x)}PbI_3$ on grid glass substrates, respectively. We further demonstrate the flexible PSCs with a promising PCE of 19.14% for small-size (1.5×1.5 cm^2) devices and an average PCE of 16.78% (the highest PCE of 18.60%) for large-area (6×6 cm^2) devices. We investigate and understand the interaction between solvents and antisolvents and derive an important guideline for fabrication of a uniform morphology for large-area perovskite solar cells.

2. Experiment

2.1 Materials

2,2′,7,7′-tetrakis(N,N-di-p-methoxyphenylamine)-9,9-spirobifluorene(Spiro-OMeTAD), lead iodide (PbI_2 99.99%) (YingKou Libra New Energy Technology Co., Ltd), $HC(NH_2)_2I$ (FAI) and CH_3NH_3Br (MABr), CH_3NH_3Cl (MACl), CH_3NH_3I (MAI) (Xi'an Polymer Light Technology Cory.), bis(trifluoromethanesulfonyl) imide (Li-TFSI), tert-butylpridine (t-BP), (Sigma–Aldrich), $SnCl_2\cdot 2H_2O$ (Alfa Aesar) were used without further purification. Dimethyl formamide (DMF, 99.8%), dimethyl sulfoxide (DMSO, 99.9%), ethyl acetate (EA), chlorobenzene (CB, 99.8%), acetonitrile and butanol were purchased from Sigma-Aldrich. EMC, dimethyl carbonate (DMC) and diethyl carbonate (DEC) were purchased from Aladdin. FTO glasses (FTO, 7 Ω/sq) were purchased from Yingkou You Xuan Trade Co. Ltd.

2.2 Preparation of SnO_2 NCs precursor

SnO_2 NCs Solution was prepared as reported before[31]. Typically, $SnCl_2\cdot 2H_2O$ solution (0.1 M) dissolved in butanol containing 5~10% (v %) content of water in a flask. Then the solution was stirred at room temperature until becoming transparent. Then, the $SnCl_2\cdot 2H_2O$ solution was refluxed at 110°C for several hours with open refluxing apparatus. Finally, a yellow and clear colloidal SnO_2 NCs solution was obtained.

2.3 *Perovskite Precursor Preparation*

$MAPbI_3$ perovskite precursor: PbI_2 (922 mg) and MAI (320 mg) were dissolved in 1.6 ml mixed solvent of DMF and DMSO (7:3 v/v), stirring at room temperature for overnight before use. $(MA)_x(FA)_yPbI_3$ based perovskite precursor: PbI_2 (742.2 mg), FAI (224.4 mg), MABr (16.2 mg) and MACl (20.3 mg) dissolved in1 ml DMSO/DMF (4:1 v/v) mixed solvent, stirring at 50°C for 2 h and keeping still for another 4 h before use.

2.4 *Devices fabrication*

FTO glass or flexible PEN/ITO was sequentially ultrasonically cleaned with detergent, deionized water and isopropanol for 15 min separately. All substrates were further cleaned by UV-Ozone for 10 min before use. The SnO_2 ETLs were deposited on substrates by spin-coating SnO_2 NCs solution at 3000 rpm for 30 s, followed by thermal annealing at 150 °C (for FTO/Glass) or 120 °C (for flexible PEN/ITO) for 0.5 h to totally remove solvent. Then, the $MAPbI_3$ precursor solution was spin-coated on FTO/SnO_2 substrates at 500 rpm for 3 s and 4000 rpm for 30s, with antisolvent quickly dripped onto the rotating perovskite film at the second spin-coating step. Then the films were annealed at 100°C for 10 min. (for MAFA based film: the dissolved precursor solution was spin-coated on the FTO/SnO_2 or PEN/ITO/SnO_2 substrates at 5000 rpm for 30 s and antisolvent was slowly dripped on the rotating substrate after the procedure start. Then the film was heated at 120 °C for 20 min to obtain a dense perovskite film. Subsequently, 17 μL HTL solution (72.3 mg spiro-OMeTAD, 17.5 μL Li-TFSI solution (520 mg in 1 ml acetonitrile), 28.8 μL t-BP) was spin-coated onto the perovskite film at 3000 rpm for 30 s. Finally, Ag electrode was thermally evaporated on the device under high vacuum ($< 4\times10^{-4}$ Pa). There are several key points in the device preparation process: 1) Control environmental temperature around 22~24°C when fabricating MAFA based rigid or flexible perovskite film; 2) Large (PEN/ITO substrate: 6×6 cm^2, active area: 0.07 cm^2) and small (PEN/ITO substrate: 1.5×1.5 cm^2, active area: 0.07 cm^2) size flexible devices were fabricated using reported method[32] to minimize efficiency loss. Typically, before fabricating perovskite solar devices, the cleaned PEN/ITO substrates were fixed on glass using double-side tape/epoxy as binders. The flexible devices were peeled off from the glass after finishing device fabrication.

2.5 *Calculation method*

In the theoretical calculation, geometry optimizations were performed using the B3LYP exchange-correlation functional with Grimme's DFT-D3(BJ) empirical dispersion correction[33]. The ma-TZVPP basis set was performed, which is the "minimally augmented" version of the def2-TZVPP basis set[34][35]. SMD solvation model was adopted. The DFT calculations were performed with Gaussian and analyzed by Multiwfn [36].

3. Results and discussion

3.1 Interaction between solvents and antisolvents

With this aim, we systematically designed three groups of experiments to understand the necessity of the typical combination between CB and N, N-Dimethylformamide (DMF), dimethyl Sulfoxide (DMSO) during the formation of $CH_3NH_3PbI_3$ perovskite film: (1) The usual condition: when DMF and DMSO as solvent ($v_{DMF} : v_{DMSO} = 7 : 3$) and CB as antisolvent dripped at 10th s and 30th s, separately, the "equivalent"-DMSO and "rich"-DMSO intermediate phases were correspondingly formed before annealing due to the fast evaporation rate of DMF. While after thermal annealing, a well-crystallized film with full coverage, and a rough film with poor coverage were obtained, respectively, as proved by the same XRD patterns but distinct SEM images (Fig. S1) [37]. (2) DMSO redundant condition: when DMF and DMSO as solvent

(v_{DMF} : v_{DMSO} = 3 : 7, to increase the DMSO content in wet film) and CB as antisolvent dripped at 10th s, we can only get the films containing lots of pin holes (Fig. S2). This phenomenon was further confirmed when the volume ratio of DMSO increases to 100% (Fig. S3). (3) DMF in antisolvent condition: when DMF and DMSO (v_{DMF} : v_{DMSO} = 7 :3) as solvent and the mixture of DMF and CB (v_{DMF} : v_{CB} = 1 :99) as antisolvent, processing window was significantly widened along with the formation of well crystalized perovskite films, as proved by the same XRD patterns, similar SEM images (Fig. S4-5).

From the above experimental results, the redundant DMSO in the wet film (before thermal annealing) is detrimental to the formation of ideal film morphology. Moreover, the inadequate DMF in the wet film is responsible for the poor morphology in accompany with the narrow processing window.

According to the recognized perovskite film forming process, antisolvent could instantly destroy the intermediate miscible state, forming the immiscibility, and evaporate afterwards together with the residue of DMF and DMSO. We thereby conducted the density functional theory (DFT) calculation of the interaction between CB, DMF and DMSO. From the determined lower binding energy of DMF−DMSO (-1.839 kJ mol^{-1}) than CB−DMSO (-1.374 kJ mol^{-1}) and CB−DMF (-1.048 kJ mol^{-1}), it suggests that the solvent extraction of DMSO (high boiling point) is primarily contributed by DMF. Thus, when CB was added beyond the processing window, more DMF (low boiling point) had evaporated, leading to the redundant DMSO left within the pre-film, which also explains the phenomenon that the addition of DMF in CB as antisolvent could widen the processing window. Thereby, it is concluded that the quantity of redundant DMSO in the pre-film is a crucial factor that determines the processing window.

Hence, we introduce a new green antisolvent —— EMC in order to offset the influence by the inadequate DMF, and consequently widen the processing window of the antisolvent washing process. Simultaneously, CB and ethyl acetate (EA) were comparatively discussed. Here we designate perovskite films with CB, EA and EMC antisolvent treatments as CB-PVK, EA-PVK and EMC-PVK, correspondingly.

The photographs of the perovskite films prepared by three antisolvents at various dripping time (5th ~ 40th s) were compared. As shown in Fig. 1a, at the range of 5th ~ 40th s, the dripping of antisolvent gives a black-mirror surface for EA and EMC antisolvent treatments, while the processing window for CB antisolvent was limited due to the formation of gray black and rough morphology. Their morphologies were further examined by scanning electron microscopy (SEM), as shown in Fig.1b and Fig. S6. The perovskite films display distinct morphologies when antisolvent dripped at 25th s, with the formed CB-PVK exhibiting messy crystalline blocks with large pinholes, and EA-PVK showing a rough morphology with obvious bumps possibly due to the excessively fast antisolvent evaporation [17,18]. In contrast, the EMC-PVK gives a dense and uniform surface. Those morphologies were further confirmed by atomic force microscopy (AFM) and X-ray diffraction (XRD) shown in Fig. S7-8 Thereby, in comparison with CB and EA, we conclude that EMC presents a wider processing window along with the formation of an ideal morphology.

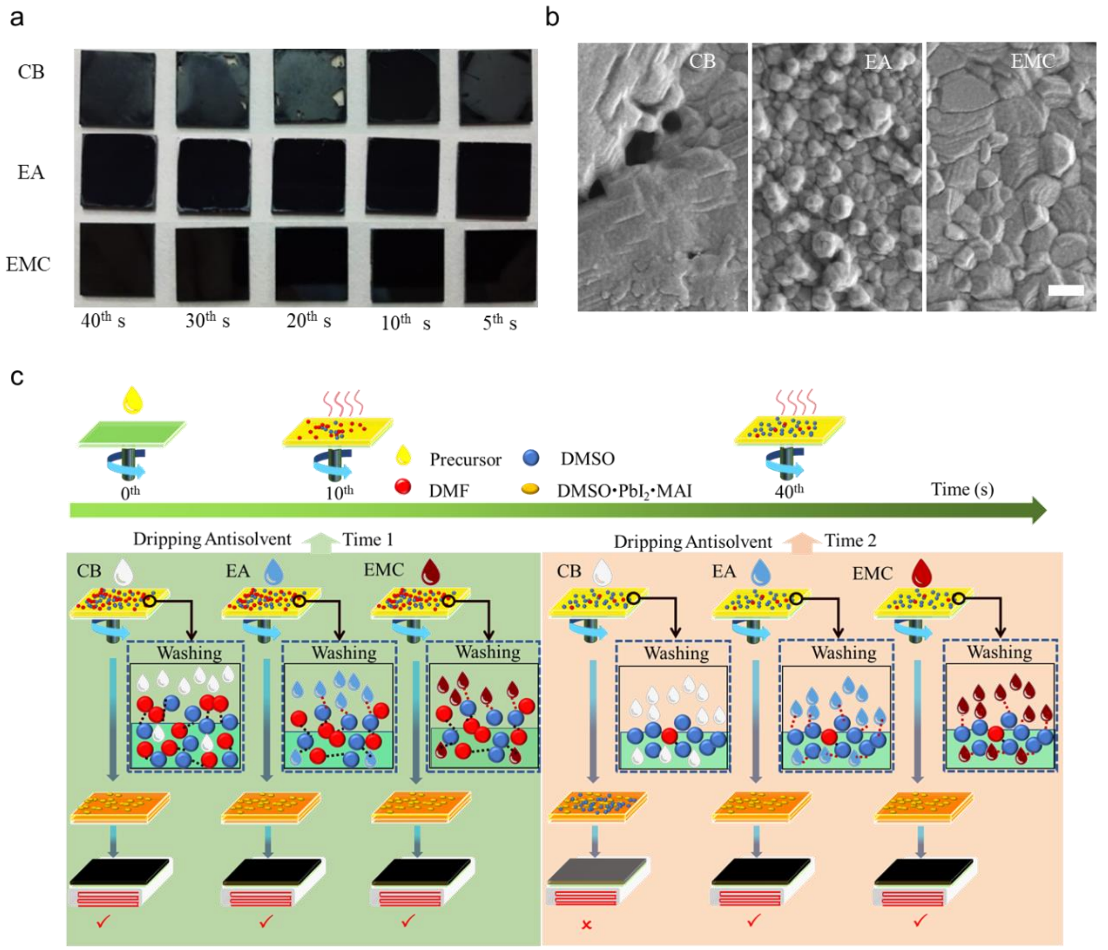

Fig. 1. Antisolvent processing window. (a) Optical photograph of the perovskite films prepared by three antisolvents at various dripping time. (b) SEM images of the perovskite films prepared by three antisolvents dripped at 25th s. (c) Scheme of the antisolvent assisted spin-coating process, all scale bars are 200 nm.

Consequently, we further proposed a solvent–antisolvent interaction hypothesis as illustrated in Fig. 1c. Generally, the spin-coating process includes three steps: (1) the physical solvent removing driven by centrifugation; (2) antisolvent dripping and (3) solvent evaporation. The narrow processing window of CB (~at 10th s to fabricate a dense and mirror–black perovskite film) is mainly attributed to the fast-changing system state. When CB was added before 10th s, too much solvent was left in the system to fulfill the rapid oversaturation; while if CB was dripped after 10th s, the inadequate residual DMF, due to its much faster evaporation rate compared with that of DMSO, could not completely extract the excess DMSO. Thus, the uncoordinated free DMSO in the pre-film would lead to the formation of inhomogeneous perovskite film with irregular stains [29–31]. However, EA and EMC antisolvents could wash uncoordinated DMSO out of the film owning to the intermolecular interaction between DMSO and their ester groups, resulting in a wider antisolvent processing window.

To verify this hypothesis, we further prepared perovskite films with pure DMSO as solvent and CB, EA or EMC as antisolvent (dripped at 10th s), respectively. From the photographs and SEM images of these perovskite films (Fig. S9), we observed considerably distinct morphologies, namely dense and uniform morphology for EA-PVK and EMC-PVK, but rough and pinholes for CB-PVK, suggesting that without the presence of DMF, EMC and EA can still extract the excess DMSO, but CB cannot.

DFT calculation was conducted to understand the interaction between solvents and antisolvents. Fig. 2a presents the binding energy of the dimer complexes, where the EMC−DMSO dimer complex shows the strongest interaction. The electron density difference maps in the inset of Fig. 2a and Fig. S10-11 (see detailed analysis in Supplementary Note 1) also illustrate the most charge transfer between the EMC and DMSO molecules, indicating the strongest interaction. In addition, the H-bond binding energies of EMC−EMC, EMC−DMF, EMC−DMSO dimer complexes based on electron density at bond critical point corresponding to H-bond were calculated (Fig. S12-13 and Supplementary Note 2), which proves that the strong EMC−DMSO interaction is attributed to the multi hydrogen bonds. On the other hand, the binding energy of EMC−DMF interaction in Fig. 2a is lower than that of DMF−DMF or EMC−EMC interaction, demonstrating that EMC antisolvent also has a good compatibility with DMF solvent.

Subsequently, the interactions of EMC−DMSO and EMC−DMF were also evaluated by Fourier transform infrared (FTIR) measurements based on EMC, DMF, DMSO and mixed solvents systems. As shown in Fig. 2b and Fig. 2c, the feature at 1283 cm^{-1} of EMC is attributed to the C−O stretching vibration, which shifts to lower wavenumbers (1280 cm^{-1} and 1277 cm^{-1}) for both EMC−DMF and EMC−DMSO mixed solvent systems, respectively. Accordingly, the feature at 1763 cm^{-1} assigned to its C=O stretching vibration shifts bathochromic to 1749 cm^{-1} and 1746 cm^{-1}, determining the strong intermolecular forces between EMC and DMSO/DMF [24,40]. In contrast, the FTIR peak has no shift for CB−DMF and CB−DMSO systems (Fig. S14), suggesting the weak interaction between CB and DMF/DMSO. Then theoretically, the infrared spectra of the antisolvent−solvent were calculated (Fig. S10-11), which is consistent with the experimental FTIR results. Moreover, the calculated bond strengths of C−O and C=O bonds (Fig. S15-16, Table S1-2 and detailed analysis in Supplementary Note 3） further validate the strong interaction between EMC with DMSO and DMF solvent.

Thus, we can chiefly understand that the quantity of DMF is critical during the

DMSO evaporation process which explains the narrow processing window based on CB antisolvent. For new antisolvent such as EMC, the interaction with DMF and DMSO, especially DMSO, could help to effectively extract the solvent and form a continuous and well-crystallized morphology, which plays a crucial role in widening the processing window.

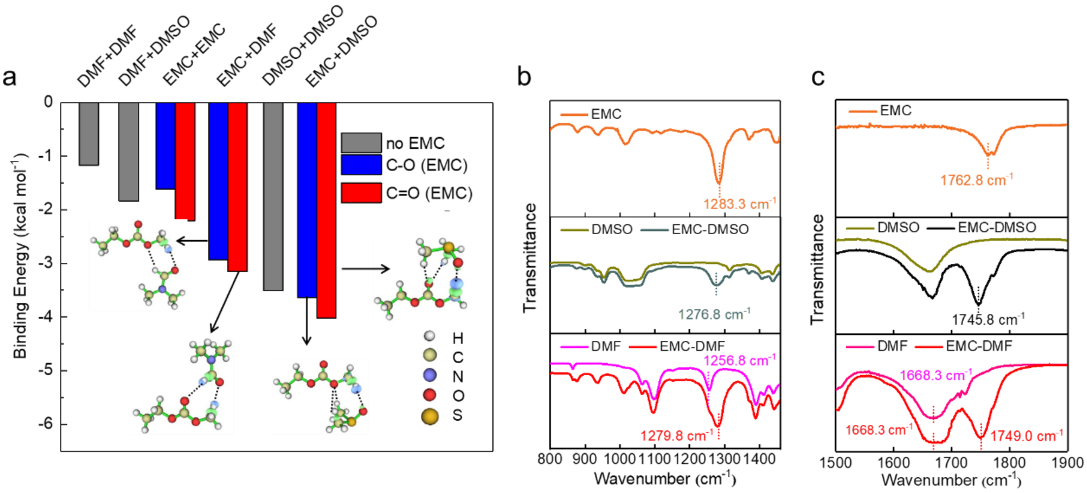

Fig. 2. Interaction between solvent and antisolvents. (a) Binding energies of dimer complexes based on the DFT calculation. The blue (red) column denotes the complex that the C−O (C=O) of EMC molecule is close to another molecule. Electron density difference maps of EMC+DMF and EMC+DMSO dimer complexes are displayed. The green and blue regions represent electron accumulation and depletion, respectively. (b) and (c), FTIR at low and high wavenumber for solvents and antisolvents.

3.2 Influence of antisolvents on the properties of perovskite films

To discuss the effects of antisolvent on the film properties, we have systematically investigated the electronic and trap states for three perovskite films. The band gap and valance/conduction band of CB-PVK, EA-PVK and EMC-PVK (estimated by ultraviolet−visible spectroscopy (UV−vis) and ultraviolet photoelectron spectrometer (UPS) in Fig. S17 show approximately equal and the negligible influence of antisolvent on electronic structures. While, except for EA-PVK with a peak shift of 0.2 eV Pb 4f , suggested by X-ray photoelectron spectra (XPS), which is related to the iodide vacancies formed during the rapid crystallization process [41,42], no obvious difference was observed for CB-PVK and EMC-PVK (Fig. S18).

The trap density of these perovskite films were further assessed by space-charge-limited current (SCLC) measurement based on the electron-only and hole-only devices [43,44]. Calculated from Fig. 3a-b, the EMC-PVK presents both lower hole-trap density (1.80×10^{16} cm^{-3}) and electron−trap density (0.48×10^{16} cm^{-3}) comparing with those of CB-PVK (1.98×10^{16} cm^{-3} and 0.61×10^{16} cm^{-3}) and EA-PVK (2.16×10^{16} cm^{-3} and 1.49×10^{16} cm^{-3}). The corresponding stronger photoluminescence (PL) of EMC-PVK than those of EA-PVK and CB-PVK (Fig. 3c) could deduce the smaller non-radiative recombination in EMC-PVK, and well matches with its lower trap density [12,45,46].

The time-resolved photoluminescence (TRPL) spectra explained the recombination details, fitted by biexponential decay function with PL lifetime (τ) using equation of $y = y_{0+} A_1 e^{{-t}/{\tau_1}} + A_2 e^{{-t}/{\tau_2}}$, in which the fast decay-time (τ_1) represents the non-radiative recombination and slow decay-time (τ_2) represents the radiative recombination from perovskite[47]. The longer τ_1 of EMC-PVK (6.87 ns) than CB-PVK (5.44 ns) and EA-PVK (4.27 ns) has been interpreted as a smaller non-radiative recombination, while its much longer average PL lifetime (τ_2) (62.19 ns) compared with that of CB-PVK (36.77 ns) and EA-PVK (31.06 ns) indicates a high-quality EMC-PVK film (Fig. 3d and Table S3) [48,49].

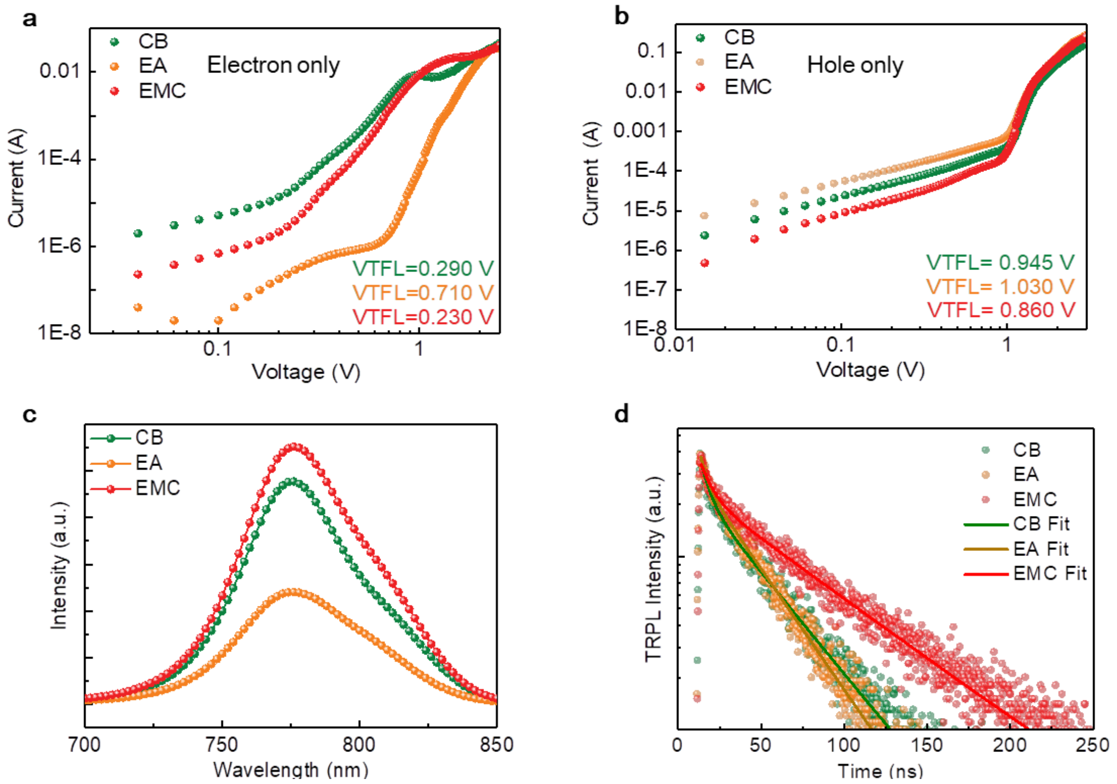

Fig. 3. Influence of antisolvents on the properties of perovskite films. (a) and (b) Electron-only and hole only SCLC curves. (c), (d) PL and TRPL of EMC-PVK, CB-PVK and EA-PVK.

3.3 Perovskite Solar Cells Performance

To thoroughly evaluate the photovoltaic performance of the obtained perovskite films from three kinds of antisolvent (dripped at 10th s), the PSCs with a planar device configuration of FTO/SnO_2/Perovskite/spiro−OMeTAD/Ag were fabricated [50]. The current density–voltage (J–V) curves with the parameters of the best PSCs are presented in Fig. 4a. The PSC using EMC-PVK exhibited a champion PCE of 21.05% along with open-circuit voltage (V_{OC}) of 1.17 V, current density (J_{SC}) of 22.61 mA cm^{-2} and fill factor (FF) of 79.85%, which significantly outperforms its counterparts with PCE of 20.18% for CB-PVK (V_{OC} of 1.15 V, J_{SC} of 22.43 mA cm^{-2} and *FF* of 78.08%) and 18.58% for EA-PVK (V_{OC} of 1.11 V, J_{SC} of 22.07 mA cm^{-2} and *FF* of 75.69%).

The external quantum efficiency (EQE) measurements were carried out to confirm the J_{SC} of devices. The integrated J_{SC} (Fig. 4b) for the PSCs based on CB, EA and EMC antisolvents treated perovskite were 21.17, 21.21 and 21.63 mA cm^{-2}, respectively, which matches well with the J_{SC} obtained from J–V curves. Moreover, the steady-state output validates their photovoltaic performances, with a corresponding stabilized PCE (obtained at the maximum power point) of 20.20%, 18.10% and 17.43% for EMC-PVK, CB-PVK and EA-PVK based cells, respectively (shown in Fig.4c).

To study the reproducibility, 23 independent cells of each antisolvent-treated PSCs were fabricated, with the statistic device parameters presented in Fig S19. The average PCE of EMC-PVK based PSCs was 19.45 ± 0.82 % with V_{OC} of 1.15 ± 0.01 V, J_{SC} of 21.92 ± 0.69 mA cm^{-2} and *FF* of 76.99 ± 1.40 %, which surpassed its counterparts with PCE of 18.78 ± 0.84 % (V_{OC} of 1.14 ± 0.2 V, J_{SC} of 21.82 ± 0.52 mA cm^{-2} and *FF* of 75.43 ± 2.42%) and 16.16 ± 0.81% (V_{OC} of 1.05 ± 0.02 V, J_{SC} of 20.78 ± 0.92 mA cm^{-2} and *FF* of 73.24 ± 3.39%) for CB-PVK and EA-PVK based cells, respectively. The higher PCE for EMC-PVK based devices mainly comes from the enhanced V_{OC} and *FF.* Meanwhile, its smaller deviation indicates that the EMC-PVK has a superior film with excellent device reproducibility.

The enhanced PSC performances were analyzed by the electrochemical impedance spectroscopy (EIS) to investigate the charge transporting dynamics. The Nyquist plots of these three kinds of PSCs give a similar internal series resistance (R_s) of 10.55, 12.51, 9.38 Ω for CB, EA and EMC-treated devices, respectively (Fig 4d). While regarding to the charge transport resistance (R_{tr}), the EMC-PVK based cell gave the lowest value (39.59 Ω) compared with that of CB-PVK and EA-PVK based cells (58.13 and 141.15 Ω), suggesting a more efficient charge transporting process in EMC-PVK based cells [51].

The large processing window of EMC antisolvent was also verified by fabricating PSCs with antisolvent (CB, EA and EMC) dripped at 5th s, 10th s, 20th s, 30th s, 40th s, respectively. From the average PCE shown in Fig. 4e and Table S4, PSCs processed by EMC antisolvent showed nearly similar average value in the range of 19.1%~19.4%, showing a wide dripping window from 5~40th s, in sharp contrast with the PSCs processed by CB, whose average PCE exhibits a significant drop from 18.5% (dripped at 10th s) to 15.2% (dripped 40th s). In addition to the antisolvent dripping time window, we have also carefully investigated the influence of DMF/DMSO ratios on device performance. In comparison, a series of ratios (7:3, 5:5, 3:7 and 0:10) of DMF/DMSO are used in perovskite precursor, then perovskite film is fabricated with CB and EMC antisolvent treatment respectively (Fig. 4f, Fig. S21 and Table S5). The devices fabricated with EMC exhibit outstanding efficiencies in the range of 19.14%~20.25%. However, the PCE of CB treated devices significantly decrease from 19.88% (V_{DMF} : V_{DMSO} = 7:3) to 7.67% (V_{DMF} : V_{DMSO} = 0:10). Those results suggest

EMC is not sensitive to the precursor solution compositions, in contrast to CB. Furthermore, the stability of the unencapsulated PSCs based on CB-PVK, EA-PVK and EMC-PVK was examined over two-weeks at the humidity around 35%, with PCEs showing a downward trend. In Fig. S22, the monitored PCEs show a similar downward trend.

To demonstrate the versatility of EMC in the perovskite films forming process, we further developed $(MA)_x(FA)_{(1-x)}PbI_3$ and $(Cs)_x(MA)_y(FA)_{1-x-y}PbI_3$ based PSCs with the device structure configuration of FTO/SnO_2/perovskite /spiro-OMeTAD/Ag. As expected, similar *J-V* parameters ($(MA)_x(FA)_{(1-x)}PbI_3$ based cells) were obtained when EMC dripped at 9th s, 17th s and 25th s, respectively (Figure S23), implying the universality of EMC antisolvent to widen processing window. Furthermore, the devices processed by EMC antisolvent achieved a satisfied PCE of 21.40% and 20.72% with respect to $(MA)_x(FA)_{(1-x)}PbI_3$ and $(Cs)_x(MA)_y(FA)_{1-x-y}PbI_3$ based solar cells.

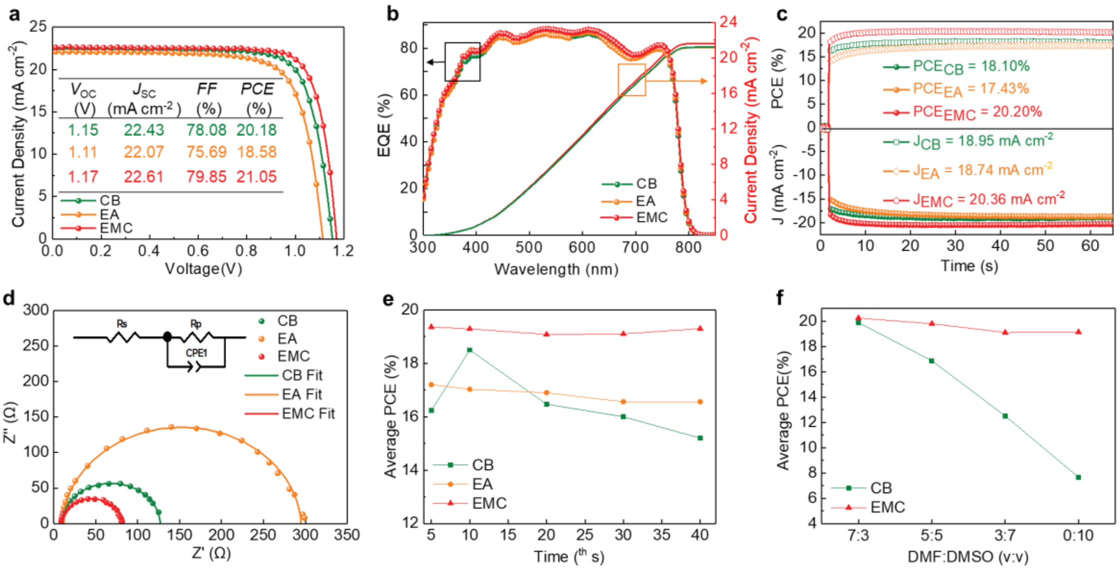

Fig.4. Performance of PSCs. (a) *J–V* curves with the inset showing detailed parameters. b) EQE

(left panel) and current density (right panel). (c) Steady PCE and current density at a constant bias voltage at V_{mp}. (d) Nyquist plots of the devices. (e) The average PCE of devices with different antisolvents dripped at different time. (f) Device performance prepared with different ratio of DMF/DMSO as precursors.

3.4 Large-area flexible solar cells

EMC has shown the great potential in widening the processing window of antisolvent, thereby presenting the promise of the fabrication of large-area flexible PSCs. We have fabricated flexible perovskite cells on a 6×6 cm^2 flexible PEN substrate and divided it into 54 subshells (active area: 0.07 cm^2) (shown in the insert of Fig. 5a). The PCE values of these 54 PSCs were summarized in Fig. 5a. The calculated average efficiency is 16.78% in the range from 15.30% to 18.60%, with a standard deviation of 0.81, revealing the good uniformity of large-area perovskite film. The corresponding small-size (1.5×1.5 cm^2) device gave a PCE of 19.14%, V_{OC} of 1.07 V, J_{SC} of 23.27 mA cm^{-2} and FF of 76.70% as shown in Fig. 5b.

Besides, the mechanical stability of flexible device was estimated under different bending curvature radii for 500 cycles. Fig. 5c shows the mechanical stability of flexible device versus different curvature radius plots, with inset exhibiting the corresponding chord distance measured by a Vernier caliper. Overall, the fabricated devices exhibit good mechanical stability, that 80% of its initial PCE was remained after accumulatively bending 2500 times.

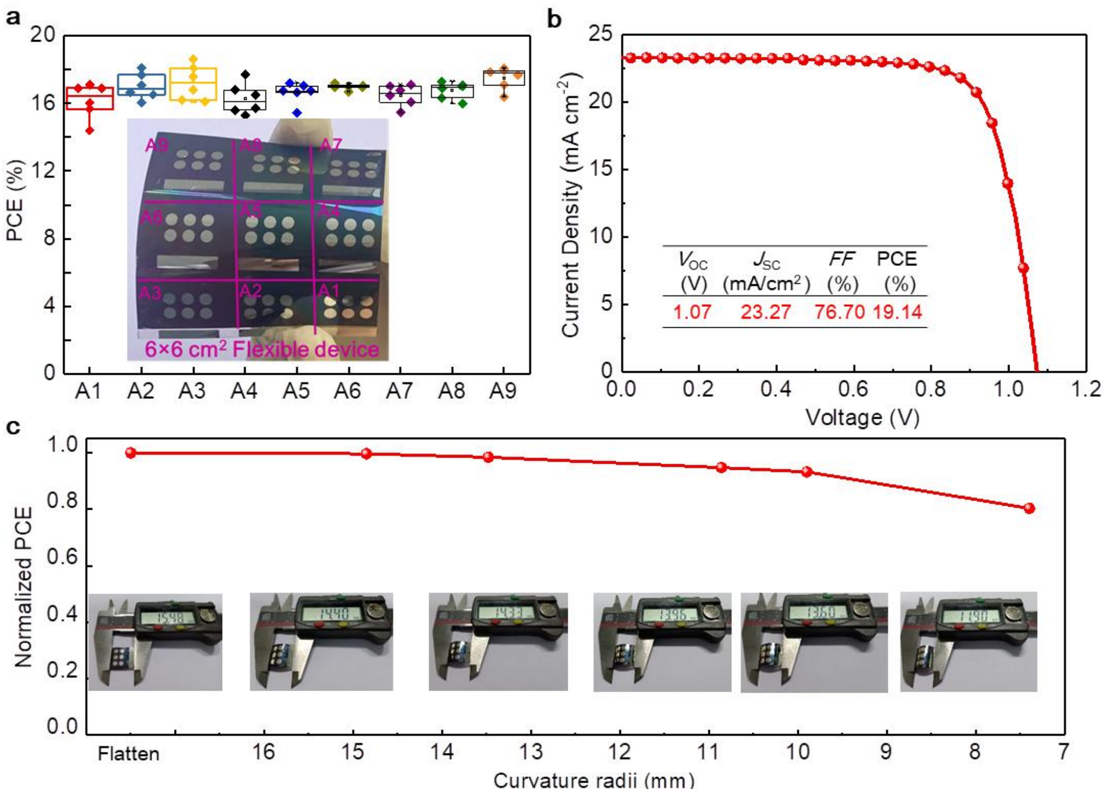

Fig. 5. Flexible PSCs performance. (a) Flexible perovskite cells based on 6×6 cm^2 flexible substrate (active area: 0.07 cm^2). (b) The best *J–V* curves of flexible devices with 1.5×1.5 cm^2 substrate. (c) The normalized PCE at different bending curvature radii after 500 cycles at each curvature radii.

4. Discussion

In summary, we have introduced an green antisolvent of EMC, which significantly widens solvent (DMF: DMSO) ratio varying from 7:3 to 0:10 in the precursor solution, as well as antisolvent processing window from 2 s to 35 s. Based on EMC antisolvent, we have achieved a maximum PCEs of 21.05% and 22.08% for $MAPbI_3$ and $(MA)_x(FA)_{(1-x)}PbI_3$ absorber devices, respectively. We further demonstrate the flexible PSCs with a promising PCE of 19.14% for small-size (1.5×1.5 cm^2) devices and an average decent PCE of 16.78% (the highest PCE of 18.60%) for large-area

(6×6 cm^2) devices. Moreover, a series carbonate antisolvents–Dimethyl Carbonate (DMC) and Diethyl Carbonate (DME) were discussed in the Supplementary Information, also presenting a desirable performance. Fig. S24−26 show black-mirror and dense perovskite film with carbonate antisolvents dripped at different time. Fig. S27 shows good film crystallinity and the XPS spectra shown in Fig. S28 indicate similar electronic structure of DMC and DME based perovskite film. Fig. S29 shows good reproducibility of efficient PSCs treated with DMC and DME antisolvents.

In parallel, the formation of perovskite film under different solvents and antisolvents was systematically investigated. We demonstrate the significant role of the typical solvent of DMF in the process of antisolvent washing, and demonstrate a solvent–antisolvent interaction model to help understand the originality of narrow processing window based on chlorobenzene (CB). Finally, we can deduce that, the strong interaction between solvent and antisolvent is an important and effective way to give a uniform morphology with wide antisolvent processing window for large-area perovskite solar cells.

Declaration of competing interest

The authors declare that they have no known competing financial interests or personal relationships that could have appeared to influence the work reported in this article.

Acknowledgement

This work is supported by NSFC Funds (U1801256, 51803064), Science and Technology Programs of Guangzhou (2019050001, 202002030130), International Cooperation Projects of

Guangdong Province (2020A0505100054), Guangdong Provincial Key Laboratory of Optical Information Materials and Technology (2017B030301007), and Collaborative Research Fund (CRF C7018-20GF) of Hong Kong Research Grants Council. We also thank the support from the Guangdong Provincial Engineering Technology Research Center for Transparent Conductive Materials.

Additional information

Supplementary information is available for this paper at https://doi.org/~

Author contributions

Cong Chen, Yue Jiang and Jinwei Gao Conceptualization, Investigation and analysis. Cong Chen and Zhuoxi Li prepared the samples and performed most of the experiments. Yancong Feng and Nengjie Cao performed the DFT calculation. Jinwei Gao, Yue Jiang, Yancong Feng, Cong Chen, and Shien-Ping Feng co-wrote the paper. All authors discussed the results and commented on the manuscript. Jinwei Gao directed the research.

References

[1] R. Wang, T. Huang, J. Xue, J. Tong, K. Zhu, Y. Yang, Prospects for metal halide perovskite-based tandem solar cells, Nat. Photonics. 15 (2021) 411–425.

[2] X. Du, J. Li, G. Niu, J. Yuan, K. Xue, W. Pan, X. Yang, B. Zhu, J. Tang, M. Xia, Lead halide perovskite for efficient optoacoustic conversion and application toward high-resolution ultrasound imaging, Nat. Commun. 12 (2021) 3348.

[3] W. Wang, R. Guo, X. Xiong, H. Liu, W. Chen, S. Hu, E. Amador, B. Chen, X. Zhang, L. Wang, Improved stability and efficiency of perovskite via a simple solid diffusion method, Mater. Today Phys. 18 (2021).

[4] S.D. Stranks, G.E. Eperon, G. Grancini, C. Menelaou, M.J.P. Alcocer, T. Leijtens, L.M. Herz, A. Petrozza, H.J. Snaith, Electron-hole diffusion lengths exceeding 1 micrometer in an organometal trihalide perovskite absorber, Science. 342 (2013) 341–344.

[5] C.C. Stoumpos, C.D. Malliakas, M.G. Kanatzidis, Semiconducting tin and lead iodide perovskites with organic cations: Phase transitions, high mobilities, and near-infrared photoluminescent properties, Inorg. Chem. 52 (2013) 9019–9038.

[6] Michael M. Lee, J. Teuscher, T. Miyasaka, T.N. Murakami, Henry J. Snaith, Efficient hybrid solar cells based on meso-superstructured organometal halide perovskites, Science. 338 (2012) 643–648.

[7] J. Burschka, N. Pellet, S.J. Moon, R. Humphry-Baker, P. Gao, M.K. Nazeeruddin, M. Grätzel, Sequential deposition as a route to high-performance perovskite-sensitized solar cells, Nature. 499 (2013) 316–319.

[8] N.J. Jeon, J.H. Noh, Y.C. Kim, W.S. Yang, S. Ryu, S. Il Seok, Solvent engineering for high-performance inorganic-organic hybrid perovskite solar cells, Nat. Mater. 13 (2014) 897–903.

[9] W.S. Yang, J.H. Noh, N.J. Jeon, Y.C. Kim, S. Ryu, J. Seo, S. Il Seok, High-performance photovoltaic perovskite layers fabricated through intramolecular exchange, Science. 348 (2015) 1234–1237.

[10] A.D. Taylor, Q. Sun, K.P. Goetz, Q. An, T. Schramm, Y. Hofstetter, M. Litterst, F. Paulus, Y. Vaynzof, A general approach to high-efficiency perovskite solar cells by any antisolvent, Nat. Commun. 12 (2021) 1–11.

[11] N.-G. Park, K. Zhu, Scalable fabrication and coating methods for perovskite solar cells and solar modules, Nat. Rev. Mater. 5 (2020) 333–350.

[12] M.M. Tavakoli, P. Yadav, D. Prochowicz, M. Sponseller, A. Osherov, V. Bulović, J. Kong, Controllable perovskite crystallization via antisolvent technique using chloride additives for highly efficient planar perovskite solar cells, Adv. Energy Mater. 9 (2019) 1803587.

[13] L. Yang, Y. Gao, Y. Wu, X. Xue, F. Wang, Y. Sui, Y. Sun, M. Wei, X. Liu, H. Liu, Novel insight into the role of chlorobenzene antisolvent engineering for highly efficient perovskite solar cells: gradient diluted chlorine doping, ACS Appl. Mater. Interfaces. 11 (2019) 792–801.

[14] F. Wang, M. Yang, S. Yang, X. Qu, L. Yang, L. Fan, J. Yang, F. Rosei, Iodine-assisted antisolvent engineering for stable perovskite solar cells with efficiency >21.3 %, Nano Energy. 67 (2020) 104224.

[15] M. Konstantakou, D. Perganti, P. Falaras, T. Stergiopoulos, Anti-solvent crystallization strategies for highly efficient perovskite solar cells, Crystals. 7 (2017) 1–21.

[16] N.J. Jeon, J.H. Noh, Y.C. Kim, W.S. Yang, S. Ryu, S. Il Seok, Solvent engineering for high-performance inorganic-organic hybrid perovskite solar cells, Nat. Mater. 13 (2014) 897–903.

[17] L. Chao, T. Niu, W. Gao, C. Ran, L. Song, Y. Chen, W. Huang, Solvent engineering of the

precursor solution toward large-area production of perovskite solar cells, Adv. Mater. 33 (2021) 2005410.

[18] S. Ghosh, S. Mishra, T. Singh, Antisolvents in perovskite solar cells: importance, issues, and alternatives, Adv. Mater. Interfaces. 7 (2020) 1–24.

[19] J. Su, H. Cai, J. Yang, X. Ye, R. Han, J. Ni, J. Li, J. Zhang, Perovskite ink with an ultrawide processing window for efficient and scalable perovskite Solar Cells in Ambient Air, ACS Appl. Mater. Interfaces. 12 (2020) 3531–3538.

[20] M. Xiao, F. Huang, W. Huang, Y. Dkhissi, Y. Zhu, J. Etheridge, A. Gray-Weale, U. Bach, Y.B. Cheng, L. Spiccia, A fast deposition-crystallization procedure for highly efficient lead iodide perovskite thin-film solar cells, Angew. Chemie - Int. Ed. 53 (2014) 9898–9903.

[21] N. Ahn, D.-Y. Son, I.-H. Jang, S.M. Kang, M. Choi, N.-G. Park, Highly reproducible perovskite solar cells with average efficiency of 18.3% and best efficiency of 19.7% fabricated via lewis base adduct of lead (II) iodide, J. Am. Chem. Soc. 137 (2015) 8696–8699.

[22] K.T. Cho, S. Paek, G. Grancini, C. Roldán-Carmona, P. Gao, Y. Lee, M.K. Nazeeruddin, Highly efficient perovskite solar cells with a compositionally engineered perovskite/hole transporting material interface, Energy Environ. Sci. 10 (2017) 621–627.

[23] Y.Y. Kim, T.Y. Yang, R. Suhonen, A. Kemppainen, K. Hwang, N.J. Jeon, J. Seo, Roll-to-roll gravure-printed flexible perovskite solar cells using eco-friendly antisolvent bathing with wide processing window, Nat. Commun. 11 (2020) 1–11.

[24] P. Zhao, B.J. Kim, X. Ren, D.G. Lee, G.J. Bang, J.B. Jeon, W. Bin Kim, H.S. Jung,

Antisolvent with an ultrawide processing window for the one-step fabrication of efficient and large-area perovskite solar cells, Adv. Mater. 30 (2018) 1–8.

[25] H.-H. Huang, Q.-H. Liu, H. Tsai, S. Shrestha, L.-Y. Su, P.-T. Chen, Y.-T. Chen, T.-A. Yang, H. Lu, C.-H. Chuang, K.-F. Lin, S.-P. Rwei, W. Nie, L. Wang, A simple one-step method with wide processing window for high-quality perovskite mini-module fabrication, Joule. 5 (2021)

[26] M. Yang, Z. Li, M.O. Reese, O.G. Reid, D.H. Kim, S. Siol, T.R. Klein, Y. Yan, J.J. Berry, M.F.A.M. Van Hest, K. Zhu, Perovskite ink with wide processing window for scalable high-efficiency solar cells, Nat. Energy. 2 (2017) 1–9.

[27] Z. Yang, W. Zhang, S. Wu, H. Zhu, Z. Liu, Z. Liu, Z. Jiang, R. Chen, J. Zhou, Q. Lu, Z. Xiao, L. Shi, H. Chen, L.K. Ono, S. Zhang, Y. Zhang, Y. Qi, L. Han, W. Chen, Slot-die coating large-area formamidinium-cesium perovskite film for efficient and stable parallel solar module, Sci. Adv. 7 (2021) 1–14.

[28] X. Kong, Y. Jiang, Z. Li, Y. Zhou, Z. Xu, C. Cong, X. Gao, X. Lu, G. Zhou, J.M. Liu, K. Kempa, J. Gao, Highly reproducible fabrication of perovskite films with an ultrawide antisolvent dripping window for large-scale flexible solar cells, Sol. RRL. 5 (2021) 2000646.

[29] L. Qiu, L. Dong, D. Mei, W.H. Chen, L. Song, J. Wang, J. Zou, P.C. Jiang, P. Du, J. Xiong, A simple fabrication of high efficiency planar perovskite solar cells: controlled film growth with methylammonium iodide and green antisolvent sec-butyl alcohol, J. Mater. Chem. C. 8 (2020)

[30] L. Wang, X. Wang, L.L. Deng, S. Leng, X. Guo, C.H. Tan, W.C.H. Choy, C.C. Chen, The mechanism of universal green antisolvents for intermediate phase controlled high-efficiency formamidinium-based perovskite solar cells, Mater. Horizons. 7 (2020) 934–942.

[31] C. Chen, Y. Jiang, J. Guo, X. Wu, W. Zhang, S. Wu, X. Gao, X. Hu, Q. Wang, G. Zhou, Y. Chen, J.M. Liu, K. Kempa, J. Gao, Solvent-assisted low-temperature crystallization of SnO2 electron-transfer layer for high-efficiency planar perovskite solar cells, Adv. Funct. Mater. 29 (2019).

[32] J. Guo, Y. Jiang, C. Chen, X. Wu, X. Kong, Z. Li, X. Gao, Q. Wang, X. Lu, G. Zhou, Y. Chen, J.M. Liu, K. Kempa, J. Gao, Nondestructive transfer strategy for high-efficiency flexible perovskite solar cells, ACS Appl. Mater. Interfaces. 11 (2019) 47003–47007.

[33] L. Goerigk, S. Grimme, Efficient and accurate double-hybrid-meta-GGA density functionals-evaluation with the extended GMTKN30 database for general main group thermochemistry, kinetics, and noncovalent interactions, J. Chem. Theory Comput. 7 (2011) 291–309.

[34] F. Weigend, R. Ahlrichs, Balanced basis sets of split valence, triple zeta valence and quadruple zeta valence quality for H to Rn: Design and assessment of accuracy, Phys. Chem. Chem. Phys. 7 (2005) 3297–3305.

[35] J. Zheng, X. Xu, D.G. Truhlar, Minimally augmented Karlsruhe basis sets, Theor. Chem. Acc. 128 (2011) 295–305.

[36] T. Lu, F. Chen, Multiwfn: A multifunctional wavefunction analyzer, J. Comput. Chem. 33 (2012) 580–592.

[37] J. Cao, X. Jing, J. Yan, C. Hu, R. Chen, J. Yin, J. Li, N. Zheng, Identifying the molecular structures of intermediates for optimizing the fabrication of high-quality perovskite films, J. Am. Chem. Soc. 138 (2016) 9919–9926.

[38] Y. Bai, S. Xiao, C. Hu, T. Zhang, X. Meng, Q. Li, Y. Yang, K.S. Wong, H. Chen, S. Yang, A pure and stable intermediate phase is key to growing aligned and vertically monolithic perovskite crystals for efficient PIN planar perovskite solar cells with high processibility and stability, Nano Energy. 34 (2017) 58–68.

[39] C.M.M. Soe, W. Nie, C.C. Stoumpos, H. Tsai, J.C. Blancon, F. Liu, J. Even, T.J. Marks, A.D. Mohite, M.G. Kanatzidis, Understanding film formation morphology and orientation in high member 2D ruddlesden–popper perovskites for high-efficiency solar cells, Adv. Energy Mater. 8 (2018) 2–11.

[40] L. Zhang, D. Zhu, H. Wang, How ethyl methyl carbonate assists ethylene carbonate in co-intercalating into graphite electrode with PF6−, J. Electrochem. Soc. 166 (2019) A2654–A2659.

[41] Y. Du, J. Wu, X. Zhang, Q. Zhu, M. Zhang, X. Liu, Y. Zou, S. Wang, W. Sun, Surface passivation using pyridinium iodide for highly efficient planar perovskite solar cells, J. Energy Chem. 52 (2021) 84–91.

[42] H. Yu, H. Lu, F. Xie, S. Zhou, N. Zhao, Native defect-induced hysteresis behavior in organolead iodide perovskite solar cells, Adv. Funct. Mater. 26 (2016) 1411–1419.

[43] Y.J. Kang, S.N. Kwon, S.P. Cho, Y.H. Seo, M.J. Choi, S.S. Kim, S.I. Na, Antisolvent additive engineering containing dual-function additive for triple-cation p-i-n perovskite solar cells with over 20% PCE, ACS Energy Lett. 5 (2020) 2535–2545.

[44] L. Liang, P. Gao, Lead-free hybrid perovskite absorbers for viable application: can we eat the cake and have it too?, Adv. Sci. 5 (2018) 1700331.

[45] X. Li, F. Cao, D. Yu, J. Chen, Z. Sun, Y. Shen, Y. Zhu, L. Wang, Y. Wei, Y. Wu, H. Zeng, All inorganic halide perovskites nanosystem: synthesis, structural features, optical properties and optoelectronic applications, Small. 13 (2017) 1–24.

[46] H. Cao, Z. Zhang, M. Zhang, A. Gu, H. Yu, H. Ban, Q. Sun, Y. Shen, X.-L. Zhang, J. Zhu, M. Wang, The effect of defects in Tin-based perovskites and their photovoltaic devices, Mater. Today Phys. 21 (2021) 100513.

[47] B. El Cohen, Y. Li, Q. Meng, L. Etgar, Dion-Jacobson Two-Dimensional Perovskite Solar Cells Based on Benzene Dimethanammonium Cation, Nano Lett. 19 (2019) 2588–2597.

[48] Y. Zhang, Y. Tu, Y. Tu, X. Yang, R. Su, W. Yang, M. Yu, Y. Wang, W. Huang, W. Huang, Q. Gong, Q. Gong, R. Zhu, R. Zhu, Green solution-bathing process for efficient large-area planar perovskite solar cells, ACS Appl. Mater. Interfaces. 12 (2020) 24905–24912.

[49] B. Li, D. Binks, G. Cao, J. Tian, Engineering halide perovskite crystals through precursor chemistry, Small. 15 (2019) 1–24.

[50] Z. Xu, Y. Jiang, Z. Li, C. Chen, X. Kong, Y. Chen, G. Zhou, J.-M. Liu, K. Kempa, J. Gao, Rapid microwave-assisted synthesis of SnO2 quantum dots for efficient planar perovskite solar cells, ACS Appl. Energy Mater. 4 (2021) 1887–1893.

[51] C.M. Tsai, N. Mohanta, C.Y. Wang, Y.P. Lin, Y.W. Yang, C.L. Wang, C.H. Hung, E.W.G. Diau, Formation of stable tin perovskites co-crystallized with three halides for carbon-based mesoscopic lead-free perovskite solar cells, Angew. Chemie - Int. Ed. 56 (2017) 13819–13823.